In vitro synthesis of amorphous Mg-, Ca-, Sr- and Ba-carbonates: what do we learn about intracellular calcification by cyanobacteria?

Nithavong Cam, Thomas Georgelin, Maguy Jaber, Jean-François Lambert, Karim Benzerara

In vitro synthesis of amorphous Mg-, Ca-, Sr- and Ba-carbonates: what do we learn about intracellular calcification by cyanobacteria?

N. Cam[a,b], T. Georgelin[a], M. Jaber[c], J-F. Lambert[a], K. Benzerara*[b]

[a]Laboratoire de Réactivité de Surface (LRS). Sorbonne Universités - UMR CNRS 7197, UPMC Univ Paris 06, 3 rue Galilée, Ivry-sur-Seine, France

[b]Institut de Minéralogie, de Physique des Matériaux, et de Cosmochimie (IMPMC). Sorbonne Universités - UPMC Univ Paris 06, UMR CNRS 7590, Muséum National d'Histoire Naturelle, IRD UMR 206, 4 Place Jussieu, F-75005 Paris, France

[c]Laboratoire d'Archéologie Moléculaire et Structurale (LAMS). Sorbonne Universités - UMR CNRS 8220, UPMC Univ Paris 06, 4 Place Jussieu, 75005 Paris, France

Corresponding author: Karim Benzerara

Institut de Minéralogie, de Physique des Matériaux et de Cosmochimie (IMPMC)

4 Place Jussieu

75005 Paris, France

Email: Karim.benzerara@impmc.upmc.fr

Phone: +33 1 44 27 75 42

Abstract

Some cyanobacteria, including *Candidatus* Gloeomargarita lithophora, which was isolated from Lake Alchichica (Mexico), can form intracellular carbonates. This contradicts the common paradigm that cyanobacterial calcification is always extracellular and suggests that calcification might be controlled by these cyanobacterial species. Intracellular carbonates have several peculiar characteristics: they are relatively small (between 60 and 500 nm), they are poorly crystalline, and they have Sr/Ca and Ba/Ca ratios much higher than the solution in which the cells grow. It is therefore crucial to understand whether these unique features may indicate the involvement of specific biological processes. Here, *in vitro* abiotic syntheses were performed to synthesize Mg-, Ca-, Sr- and Ba-containing carbonates with compositions, crystallinities and sizes close to those observed in intracellularly calcifying cyanobacteria. Precipitates were characterized by scanning and transmission electron microscopies coupled with energy dispersive x-ray spectroscopy, thermogravimetric analysis and x-ray diffraction. The size and the poor crystallinity of cyanobacterial intracellular carbonates could be mimicked under these abiotic conditions. It was shown that similarly to Mg, elements such as Sr and Ba can favour stabilization of poorly crystalline carbonates. In contrast, the differential partitioning of Sr, Ba and Ca between the solution and the solids as observed in cyanobacteria could not be mimicked *in vitro*. This provides keys to a better understanding of biological processes involved in the formation of intracellular carbonates by some cyanobacteria, including the involvement of membrane transporters.

1. INTRODUCTION

Cyanobacteria are photosynthetic prokaryotes that occupy a wide array of terrestrial, marine, and freshwater habitats (Badger et al., 2006). They contribute significantly to the global carbon cycle by assimilating CO_2 to organic carbon (Fuhrman, 2003) and by triggering $CaCO_3$ precipitation (e.g., Verrecchia et al., 1995; Kamennaya et al., 2012).

The general reaction of $CaCO_3$ precipitation can be written as:

$$Ca^{2+}{}_{aq} + CO_3^{2-}{}_{aq} = CaCO_{3,\,solid} \qquad (1)$$

This is coupled with the acid-base equilibrium of carbonates, e.g.

$$2\,HCO_3^{-}{}_{aq} = CO_3^{2-}{}_{aq} + CO_{2\,aq} + H_2O \qquad (2),$$

Therefore, the $CaCO_3$ precipitation reaction can be written alternatively as

$$Ca^{2+}{}_{aq} + 2HCO_3^{-}{}_{aq} \rightarrow CaCO_{3,\,solid} + CO_{2,\,aq} + H_2O \qquad (3)$$

with (3) = (1) + (2)

Cyanobacteria impact that reaction by fixing CO_2 through photosynthesis, hence displacing equilibrium (3) towards the formation of $CaCO_3$. More precisely, cyanobacteria usually import carbon under the form of HCO_3^- especially in environments where dissolved CO_2 is limiting. HCO_3^- is then converted to CO_2 within cell compartments called carboxysomes by specific enzymes, i.e. carbonic anhydrases (Kupriyanova and Pronina, 2011). CO_2 is then fixed by the RuBisCO enzyme and transformed into organic carbon while CO_3^{2-} and/or OH^- produced by the carbonic anhydrase reaction are exported to the extracellular medium (e.g., (Kamennaya et al., 2012)). This raises the supersaturation of the surrounding solution with respect to various carbonate minerals. An additional source of oversaturation is provided by an active export of Ca^{2+} from the cells coupled with an import of H^+ (Thompson et al., 1997).

Until recently, calcification by cyanobacteria has been invariably considered as an extracellular process (Merz, 1992). As a result, the $CaCO_3$ precipitation process and the chemical composition of the mineral by-products were supposed to be influenced only by the chemical conditions prevailing in the aqueous environment at the cell/solution interface.

However, several species of cyanobacteria have been discovered recently that have the ability to form intracellular carbonate inclusions (Couradeau et al., 2012; Benzerara et al., 2014). Despite the potential importance of such a process (Couradeau et al., 2012; Riding, 2012; Benzerara et al., 2014), the mechanisms involved in the formation of intracellular carbonates by cyanobacteria are as yet unknown. These intracellular carbonates are quite different from usual abiotic carbonates: (1) they appear as nanospheres with a diameter between 60 and 500 nm; (2) they are poorly crystalline as inferred by electron diffraction; (3) in some species, e.g., *Candidatus* Gloeomargarita lithophora, they contain high concentrations of strontium and barium, much higher than in the extracellular solution. For example, the Sr/Ca and Ba/Ca ratios in the intracellular carbonates of *Candidatus* G. lithophora were respectively 86 and 1370 times higher than in the extracellular solution (Couradeau et al. 2012). Interestingly, similarly to what has been observed in *G. lithophora*, an enrichment in Sr and Ba relative to Ca was observed recently in carbonates from the water column of Lake Geneva (Switzerland) by (Jaquet et al., 2013).

The origin of such a high enrichment in Sr and Ba relative to Ca in intracellular precipitates, as well as the mechanism by which such poorly crystalline carbonates are stabilized in cyanobacteria have yet to be determined. In particular, it is crucial to ascertain whether they are indicative of a biological control or the result of non-controlled processes occurring under specific chemical conditions within the cytoplasm of the cells. In turn, relating the chemical and crystallographic features of such inclusions with the chemical environment in which they formed may provide a new approach to constrain the chemical composition of the cytoplasm

in microorganisms. *In vitro* experiments have been classically performed for more than 50 years to better understand biomineralization processes (Kitano and Hood, 1965). Such modelling experiments do not intend to mimic the processes occurring within the cells, which remain unknown, and generally do not provide an ultimate and direct answer as to which biological processes are involved in biomineralization. Yet, these experiments constrain to some extent the chemical conditions necessary to produce mineral phases *in vitro* similar to those observed in organisms.

In the present study, we have conducted abiotic precipitation experiments under various conditions and we have systematically analyzed the solid products by x-ray diffraction (XRD), scanning and transmission electron microscopies (SEM and TEM) and thermogravimetric analyses (TGA) with the objective to mimic some of the chemical and crystallographic properties observed in cyanobacterial intracellular carbonates. From the comparison between the *in vitro* abiotic precipitates and cyanobacterial inclusions, we discuss the implications for intracellular carbonate biomineralization.

2. MATERIAL AND METHODS

2.1 Carbonate syntheses

Carbonates were synthesized by direct precipitation in aqueous solutions containing $MgCl_2$, $CaCl_2$, $SrCl_2$, $BaCl_2$ and Na_2CO_3 or $NaHCO_3$. Solutions of $MgCl_2.6H_2O$ (PROLABO, 98%), $CaCl_2$ (PROLABO, 99%), $SrCl_2.6H_2O$ (PROLABO, 99%), $BaCl_2.2H_2O$ (MERCK, 99%) and $NaHCO_3$ (SIGMA ALDRICH, 99.5%) were prepared separately. The Na_2CO_3 solution was added to the cation solution (i.e., a mixture of $MgCl_2$ and/or $CaCl_2$ and/or $SrCl_2$ and/or $BaCl_2$ with varying ratios) while stirring. In one experiment, $NaHCO_3$ was added to the cation solution. The pH of the different experiments are reported in Table 1. For each experiment, a

white precipitate appeared instantaneously. The suspension was then centrifuged for 10 minutes at 8200 g and the supernatant was discarded. The pellet was spread on a Petri dish and dried at room temperature.

2.2 Saturation indices calculation

Saturation indices were calculated using the Visual Minteq 3.0 software. They correspond to the logarithm of the ion activity product divided by the solubility product of the mineral phase of interest. The solubility product of amorphous calcium carbonate used in the present study was obtained by Kellermeier et al. (2014).

2.3 Scanning electron microscopy coupled with energy dispersive x-ray spectrometry

Scanning electron microscopy (SEM) images were obtained on gold-coated samples using a Hitachi SU-70 SEM-FEG equipped with a field emission gun. Images were acquired with the microscope operating at 10 kV, and a working distance of ~15 mm in the secondary electron mode using a SE (Lower) detector. Energy dispersive x-ray spectrometry (EDXS) analyses were performed using a Zeiss Ultra 55 SEM-FEG on carbon coated samples at 10 kV and a working distance of ~7.5 mm. The spot size was about 50 nm with a total acquisition time of 5 seconds. Around ten acquisition areas were used for each sample to determine the average composition. Semi-quantitative analysis of EDXS data was performed with the INCA software using a XPP matrix correction and reference spectra acquired on standard samples. The Kα lines of Mg and Ca and Lα lines of Sr and Ba were used for quantification.

2.4 Transmission electron microscopy

Transmission electron microscopy (TEM) analyses were performed in the bright field mode using a JEOL 2100F operating at 200 kV and equipped with a field emission gun, a high-resolution UHR pole piece, and a Gatan energy filter GIF 200. Samples were prepared as fine

powders by grinding in absolute ethanol in a mortar. Three microliters of this suspension were deposited on a copper grid covered with a carbon membrane.

2.5 X-ray diffraction

Bulk samples were analyzed by x-ray diffraction (XRD). A few milligrams of the samples were ground in an agate mortar in pure acetone. Powders were deposited on monocrystalline silicon sample holders. XRD measurements were performed using the Cu Kα radiation on a Panalytical X'Pert Pro MPD diffractometer. The following settings were used: the Soller slit was open at 0.04 rad; a beam mask of 20 mm, a divergence slit of 1/4 ° and an anti-scatter slit of 1/2 ° were inserted. Data were recorded at 40 kV and 40 mA in the 2θ continuous-scan mode over a 4-120° 2θ range with a step of 0.017° and a total counting time of ~5 h. XRD data were analyzed using the Panalytical X'Pert Highscore software for background subtraction.

2.6 Thermogravimetric analysis-Differential scanning calorimetry

Thermogravimetric analysis-Differential scanning calorimetry (TGA-DSC) analyses were performed using a SDT Q 600 TA. Around 10 mg of powder were placed in an aluminum crucible and the sample was heated up to 900 °C under a 100 mL/min air flow. The temperature scanning rate was set at 5 °C per minute.

2.7 Mass spectrometry

The mass spectrometry analyses were coupled with the TGA-DSC analyses on a ThermoStar^{TM} GSD 301 T3 (Pfeiffer Vacuum). The signal corresponding to 44 amu (CO_2^+) was recorded.

3. RESULTS

In a first experiment, called "stoichiometric conditions", $MgCl_2$, $CaCl_2$, $SrCl_2$, $BaCl_2$ and Na_2CO_3 were mixed in a solution with relative proportions similar to those measured by SEM-EDXS by Couradeau et al. (2012) in *G. lithophora* intracellular inclusions (i.e., Mg = 18%, Ca = 53%, Sr = 8%, Ba = 21%, in atomic ratios relative to the total cation content). Moreover, concentrations were set so that $[Na_2CO_3] = [CaCl_2] + [BaCl_2] + [SrCl_2] + [MgCl_2]$ = 100 mM (Table 1).

A second experiment was performed also under "stoichiometric conditions" at lower concentrations, i.e. with $[CO_3] = [Ca] + [Ba] + [Sr] + [Mg]$ = 10 mM.

Finally, the relative proportions of Ca, Mg, Sr and Ba added to the solution were varied to test the impact of such compositional variations of the solution on the crystallinity and chemical composition of resulting precipitates.

3.1. Precipitation of *G. lithophora*-like carbonates under stoichiometric conditions at high carbonate concentration (100 mM)

The precipitate formed in the presence of a total carbonate ion concentration of 100 mM (provided as Na_2CO_3) and dried at 20 °C without prior rinsing, was composed of particles measuring 48 ± 19 nm in diameter (measured on 146 particles). The precipitates contained Ca, Mg, Sr, Ba in the same relative proportion as in the initial solution (Fig. 1). The diffractogram revealed the presence of two phases: (1) a poorly crystalline phase with broad peaks centered at 30°, 45° and 65° (2θ) attributed to a (Ca-, Mg-, Sr-, Ba)-carbonate phase consistently with TEM observations and former XRD analyses of amorphous calcium carbonates (ACC), and (2) a crystalline phase with narrow peaks centered at 27.4°, 31.7°, 45.5°, 56.5°, 66.3° and 75.3° (2θ), assigned to NaCl. When collected one month, instead of few minutes, after the mixing of the solutions, the precipitate showed a similar diffractogram, suggesting that the poorly crystalline (Ca, Mg, Sr, Ba)-carbonate phase was relatively stable

over time. When the synthesis was performed at a lower initial pH of 8.77, with carbonates provided as $NaHCO_3$, precipitation occurred slower and the precipitate was a crystalline (Ca, Sr, Ba)-carbonate containing low amounts of Mg (Fig. 2).

TGA-DSC analyses of the poorly crystalline precipitates formed in Na_2CO_3-containing solutions showed four weight loss events (Fig. 1). The first event with a maximum at 77 °C was attributed to the loss of adsorbed and/or structural water. The peak extended up to about 300 °C, indicating that part of this water was strongly retained. The total water content amounted to 20% of the weight of the solid remaining at 300 °C. Overall, this corresponded to a water content of 0.86 water molecule per carbonate. Therefore, by coupling the TGA and EDXS data (Fig. 1), the stoichiometric formula of the precipitate could be written as $Mg_{0.16}Ca_{0.51}Sr_{0.08}Ba_{0.25}CO_3 \cdot 0.86H_2O$.

The second loss event showed a sharp maximum at 345 °C. It was associated with CO_2 release as followed by mass spectrometry and a strongly exothermic event as shown by DSC. The total weight loss during this event amounted to 3.7 to 4.0% of the dry weight. Therefore, this event could be interpreted as a partial decomposition (11-12%) of the carbonates.

A third weight loss was observed between 500 and 700 °C. It also closely matched CO_2 release but it was associated with a clear endothermic effect on the heat flow curve. This loss amounted to 16.5 to 17.7% of the dry weight, i.e., 47 to 51% of total carbonate.

Overall, the amount of carbonate decomposed in the second event (T_{max} = 345 °C) roughly corresponded to the Mg content of the solid phase, while the amount decomposed in the third event (T_{max} = 637 °C) closely corresponded to its Ca content, suggesting a multi-step carbonate decomposition ($MgCO_3$ first; $CaCO_3$ second; $SrCO_3$ and $BaCO_3$ above 710 °C). XRD analyses were performed on the solid phase before and after the second weight loss event, at 325 °C and 375 °C, respectively (Fig. 1). An increased amount of calcite was detected at 375 °C, suggesting that the initially amorphous mixed carbonate crystallized at

345 °C, causing the segregation of $MgCO_3$ which decomposed at this temperature. The start of a fourth weight loss above 710 °C and not completed at 800 °C, might be consistent with the decomposition of a residual (Sr,Ba)-carbonate phase.

3.2. Precipitation of *G. lithophora*-like carbonates under stoichiometric conditions at low carbonate concentration (10 mM)

Syntheses were carried out using lower total concentrations of carbonate anions and divalent cations (10 mM instead of 100 mM). The relative proportions of Mg, Ca, Sr and Ba were kept similar to those measured in *G. lithophora* intracellular inclusions (Table 1). The resulting precipitate was not rinsed and was dried at 20 °C. The precipitate showed a broad XRD diffraction peak around 30° (2θ), consistent with a poorly crystalline (Ca, Sr, Mg, Ba)-carbonate phase (Fig. 3). No NaCl was detected, likely due to the lower reactant concentrations. TEM observations showed that it was composed of spheres with an average diameter of 126 ± 32 nm (measurements on 385 particles; Fig. 3). Based on TGA and EDXS analyses, the average chemical composition of the precipitate was determined to be $Mg_{0.04}Ca_{0.61}Sr_{0.06}Ba_{0.29}CO_3 \cdot 0.84H_2O$. The precipitate contained much lower Mg than the solid formed at high carbonate and divalent cation concentrations. In contrast, the water content and the relative Sr/Ca, and Ba/Ca ratios were similar.

In TGA, water loss occurred in two steps at low temperatures, and the main weight loss event occurred at 670 °C. An exothermic event, not associated with weight loss was recorded at 354 °C by TGA-DSC (Fig. 3) and was attributed to crystallization of the carbonate phase without decarbonatation. This contrasted with what was observed for the precipitate formed at high

carbonate and divalent cation concentrations, for which crystallization was associated with the decomposition of $MgCO_3$.

Rinsing with milliQ water induced the transformation of the poorly crystalline phase into a substituted calcite phase as shown by XRD (Fig. 3). Moreover, when collected one month instead of few minutes after mixing the solution, the precipitate consisted mostly in crystalline calcite with a small amount of monohydrocalcite as shown by XRD (Fig. 3).

3.3. Precipitation of carbonates at low carbonate concentration and varying Sr/Ca/Mg and Ba relative proportions

To test whether a poorly crystalline Mg-rich carbonate phase could be formed at low carbonate concentration ($[CO_3^{2-}]$ = 10 mM), an additional synthesis was performed in a solution containing a higher Mg^{2+} concentration, with the following molar ratios: Mg: 55%, Ca: 29%, Sr: 4% Ba: 12% (Table 1). The precipitate appeared by TEM as spheres larger than in the previous syntheses, with an average diameter of 192 ± 44 nm as measured on 178 particles (Fig. 4). The elemental composition was $Mg_{0.16}Ca_{0.51}Sr_{0.05}Ba_{0.28}CO_3$, i.e. close to the precipitate formed in the experiment at high carbonate and divalent cation concentrations (100 mM). The XRD pattern indicated that the precipitate was poorly crystalline. TGA analyses showed a relatively high water amount of 1.03 molecules per carbonate with two distinct water loss events at 80 and 220 °C. DSC indicated an exothermic crystallization event at 370 °C, which was immediately followed by a small CO_2 loss (corresponding to the decomposition of 0.02 carbonate per formula unit). The main decarbonatation event, corresponding to the decomposition of 0.61 carbonate per formula unit, showed a maximum at 670 °C.

Additionally, syntheses were conducted without adding (1) Mg, (2) Sr, (3) Ba or (4) Sr and Ba in the solution in order to assess the influence of these elements on the size and the crystallinity of the precipitates.

In the absence of Mg^{2+} in the solution, particles were much larger (4-5 µm) than in previous syntheses (Fig. 5). Their elemental composition was close to that of the solution, with no preferential incorporation of Ca, Sr or Ba in the solid (Table 1). The precipitate consisted in well-crystallized calcite substituted by Sr and Ba (Fig. 5), with the following stoichiometry: $Ca_{0.59}Sr_{0.07}Ba_{0.34}CO_3$. TGA analyses showed the presence of only minor amounts of physisorbed water (1.4% in weight) and decarbonatation occurred between 500 and 700 °C (corresponding to the decomposition of 0.60 carbonates per formula unit).

When no Sr or Ba was added to the solution, precipitates appeared as spheres with a diameter of 181 ± 46 nm and 268 ± 61 nm, respectively (Fig. 6-7). These spheres were poorly crystalline as shown by XRD. Similarly to all other experiments, no differential partitioning of Ca, Ba and Sr was evidenced between the solution and the precipitate. The Sr-free sample contained 0.93 water molecules per carbonate (Fig. 6) and showed a crystallization peak at 379 °C. The Ba-free sample contained 0.88 water molecules per carbonate and no crystallization was detected on the heat flow curve (Fig. 7). In both cases, the precipitates crystallized when left in solution for one month. The synthesis with Sr resulted in the formation of a monohydrocalcite phase (Fig. 6) and the synthesis with Ba resulted in a mix of monohydrocalcite and aragonite phases (Fig. 7). Finally, monohydrocalcite formed when neither Sr nor Ba was added to the initial solution (Fig. 8). The precipitate appeared as spherulites measuring between 4 and 5 µm in diameter. Monohydrocalcite contained around 25 at% of Mg.

4. DISCUSSION

Over the last twenty years, amorphous calcium carbonates (ACC) have been increasingly detected in diverse samples, including biomineralizing systems (e.g., Gebauer et al., 2008; Weiner and Addadi, 2011; Cartwright et al., 2012). It has been shown that ACC are relatively unstable with an enthalpy of crystallization of -17.1 ± 0.7 kJ/mol (Radha et al., 2012), and a high solubility product, i.e 2.32 ± 0.41 $x10^{-8}$ M^2 at pH 9 (Kellermeier et al., 2014). Magnesium, some phosphorylated amino acids (Bentov et al., 2010), serine- and glycine-rich proteins (Aizenberg et al., 1996) as well as confinement (Stephens et al., 2010) have been shown to stabilize ACC. Therefore, these different parameters, i.e., high Mg contents, presence of biomolecules or confinement within intracellular vesicles, may play a role in the stabilization of amorphous carbonate inclusions within intracellularly calcifying cyanobacteria. Alternatively, the high Sr and Ba contents might be additional drivers but no previous study has investigated that potential effect. In the following sections, we compare the results obtained on synthesized amorphous Ca-, Mg-, Sr- and Ba-containing carbonates with previous studies which focused mostly on ACC and amorphous magnesium carbonates (AMC). We then discuss the implications on our understanding of the mechanisms involved in intracellular carbonate formation by cyanobacteria.

4.1 Formation of amorphous Ca-, Mg-, Sr- and Ba-carbonates

In the present study, we reported the formation of an amorphous Ca-, Sr-, Ba- and Mg-containing carbonate. This phase contained around one molecule of water per carbonate similarly to what has been often observed in abiotic (Brečević and Nielsen, 1989; Michel et al., 2008; Radha et al., 2010; Radha et al., 2012) and biogenic (Levi-Kalisman et al., 2000) ACC. This water content corresponds to that of « type 1 » ACC, observed in the early stage of sea urchin spicule biomineralization (Politi et al., 2008).

The formation and stabilization of ACC (Gebauer et al., 2010; Fernandez-Martinez et al., 2013; Ihli et al., 2013a), AMC (Jiang et al., 2010; Radha et al., 2012; Liu et al., 2013) and amorphous iron (II) carbonate (AFC, Sel et al., 2012) have been widely studied. Similarly to what has been described for ACC and AMC, amorphous (Ca, Sr, Ba, Mg)-carbonates were fairly unstable as shown by the fact that quick milliQ water rinsing induced their crystallization into a Mg-, Sr- and Ba-substituted calcite.

The crystallization temperature of amorphous Ca-, Mg-, Sr- and Ba-carbonates synthesized in the present study ranged between 345 and 390 °C, which is compatible with the 320-350 °C temperature range measured at higher temperature scanning rates for various ACC and AMC by previous studies (Koga et al., 1998; Radha et al., 2010; Radha et al., 2012; Ihli et al., 2013b). It should be noted that the variations of the crystallization temperature were not correlated with (1) the proportions of Mg, Ca, Sr, or Ba, (2) the amount of water molecules per carbonate or (3) the pH of the precipitating solutions. Alternatively, such variations may parallel the variations of the average size of the precipitates, with crystallization temperature increasing with the particle size, although uncertainties on particle sizes are high. Modelling of prenucleation of nanoparticles suggests that particle stability increases with growing diameter, which supports the present observations (Navrotsky, 2004; Gebauer et al., 2008; Meldrum and Sear, 2008; Raiteri and Gale, 2010). However, Koga et al. (1998) observed the opposite effect: the crystallization temperature actually increased with the decrease of the particle size (and it increased with the pH of the precipitating solution). The crystallization temperature may thus depend on related but different parameters such as the supersaturation of the precipitating solution. A possible explanation for the discrepancies between the cited studies might be the effect of Mg adsorbed on the particles surface, since Ihli et al. (2013b) showed that addition of Mg in the precipitation solution had a strong effect on the temperature of crystallization of the ACC. Mg is known to inhibit calcium carbonate crystallization and to

favor ACC (Loste et al., 2003; Rodriguez-Blanco et al., 2012). The intensity of inhibition was shown to depend on the Mg/Ca ratio of the precipitating solution. For example, Loste et al. (2003) showed that in a solution with a 4:1 Mg:Ca ratio, the precipitate crystallized in less than 30 min, while a 10:1 Mg:Ca ratio was required to preserve ACC for more than 24 h. In our study, the Mg:Ca ratio was less than 2:1 in several experiments where amorphous carbonates precipitated. Interestingly, the addition of Sr or Ba to a Mg- and Ca-containing solution (same initial [Mg] and $[CO_3]$:[Ca] ratio) resulted in the formation of an amorphous phase (Fig. 6-8). In contrast, the synthesis with only Ca, Sr and Ba and no Mg resulted in the formation of crystalline calcite (Fig. 5). Overall, these observations show that, although Sr and Ba alone do not induce the formation of amorphous carbonates, they increase the stability of the amorphous phase, synergistically in the presence of Mg.

4.2 Relative partitioning of Sr, Ba and Ca between the solution and the precipitates

Many studies have examined the partitioning of Sr and Ba compared to that of Ca between the solution and different crystalline calcium carbonate phases (Kinsman and Holland, 1969; Lorens, 1981; Mucci and Morse, 1983; Pingitore Jr. and Eastman, 1986; Tesoriero and Pankow, 1996; Dietzel and Usdowski, 1996; Dietzel et al., 2004; Rimstidt et al., 1998). However, most of them used conditions very different from ours for Ca-carbonate precipitation, including low precipitation rates over several hours, seawater-like solutions and/or trace concentrations of Sr or Ba, less than 1000 ppm. Under such conditions, a differential partitioning between the solution and calcite was observed for Sr or Ba vs. Ca: the Sr/Ca and Ba/Ca ratios in substituted calcite were significantly lower than in the solution, e.g., a ratio of 0.021 between Sr/Ca in the solid and Sr/Ca in the solution, and 0.012 between Ba/Ca in the solid and Ba/Ca in the solution at 25 °C (Tesoriero and Pankow, 1996). In contrast, the (Sr,Ba)-calcite synthesized in the present study contained similar Sr/Ca and

Ba/Ca ratios as in the solution. This might be explained by the substantially higher precipitation rates achieved in our experiments (Gebrehiwet et al., 2012). The differential partitioning of Ca, Sr and Ba between the solution and aragonite synthesized by CO_2 diffusion at pH 9 and a [Mg]:[Ca] of 2:1 ([Mg] = 10 mM) was significantly different, as reported in the literature: Sr/Ca and Ba/Ca ratios have been shown to be almost equal in aragonite and its precipitation solution at 25 °C, but lower in aragonite than in the solution when the temperature was increased (Dietzel et al., 2004). For example, the distribution coefficient of Sr, defined as the ratio between Sr/Ca in the solid and Sr/Ca in the solution, was measured as 1.19 in aragonite at 25 °C. The distribution coefficient of Ba was estimated at 1.5 under the same conditions (Dietzel et al., 2004).

So far, no study has assessed the distribution coefficient of Sr and Ba in amorphous carbonates. In the present study, the amorphous carbonate forming at 20 °C had a smaller Sr/Ca ratio than the solution (i.e., a distribution coefficient between 0.7 and 1) and a higher Ba/Ca ratio than the solution (distribution coefficient between 1.2 and 1.4). To the first order however, these distribution coefficients of Ba and Sr between the solution and an amorphous carbonate phase are not much different from those measured for crystalline aragonite and relatively close to 1.

4.3 Implications for intracellular precipitation in *G. lithophora*

The mechanism of amorphous (Ca, Mg, Sr, Ba)-carbonate precipitation within the cytoplasm of intracellularly calcifying cyanobacteria, including *G. lithophora,* is not known yet. Genomic and genetic approaches may provide some crucial keys in the future. However, the particular chemical and crystallographic properties of the carbonate inclusions should also help constraining the conditions under which precipitation occurs. One difficulty in inferring why some cyanobacteria form intracellular carbonates and others do not, is the very limited available information on the chemical composition of the intracellular medium in

cyanobacteria. Most of the studies usually assess that Ca^{2+} concentration in the cytoplasm is tightly regulated at very low concentrations. For example, Barrán-Berdón et al. (2011) measured an intracellular Ca^{2+} concentration of 100 nM in *Anabaena* sp. PCC 7120 cells (which do not form intracellular carbonates; Benzerara et al. (2014)), with a peak at 2.6 µM during few seconds when the cells were exposed to environmental pollutants. Such low concentrations are not consistent with the conditions used in our experiments but also incompatible with the formation of intracellular amorphous carbonate inclusions. Indeed, consistently with previous studies on ACC and AMC, the present study stresses the need for high supersaturation levels for the formation of amorphous Ca-, Sr-, Ba- and Mg-carbonates. It can therefore be noted that no valid estimation of intracellular Ca^{2+} concentrations is presently available for intracellularly calcifying cyanobacteria. Interestingly, Yu and Margolin (1997) suggested that relatively high concentrations of free Ca (a few mM) are required at least temporarily in the cytoplasm of *Escherichia coli* to allow polymerization of the tubulin-like protein FtsZ. They encountered the same paradox as in the case of intracellularly calcifying cyanobacteria: while intracellular free Ca concentrations are low, processes such as ACC precipitation require much higher concentrations. Only precise, time- and space-resolved measurements of intracellular free Ca concentration will be able to solve that issue in the future. Badger and Andrews (1982) measured a total inorganic carbon content (mostly corresponding to HCO_3^-) in excess of 30 mM within the cells of *Synechococcus* sp. Nageli RRIMP N1. This is in the same order of magnitude as inorganic concentrations used in the present study. Finally, pH is another issue which determines which major inorganic carbon species is prevalent. Several studies have measured the intracellular pH of diverse cyanobacterial strains. For example, Belkin and Boussiba (1991) measured a pH between 6.8 and 7.9 in *Arthrospira platensis*. Jiang et al. (2013) measured an intracellular pH between 6.9 and 7.5 in a wild type and a mutant strain of *Synechocystis* sp. PCC 6803. These

cyanobacterial strains do not form intracellular carbonates (Benzerara et al., 2014). Similarly to calcium concentration, pH was much higher in our in vitro syntheses than in these studies. Future studies will have to determine whether intracellularly calcifying cyanobacteria have specifically a higher intracellular pH than noncalcifying cyanobacteria, or alternatively whether pH can be locally much higher than in the rest of the cytoplasm of these cells.

Some studies have shown the positive effect of confinement on the stabilization of ACC by limiting the contact between amorphous carbonates and the surrounding solution (Stephens et al., 2010). Other studies have shown the stabilization of amorphous carbonates by specific macromolecules, including glycoproteins, polyphosphate or phosphorylated proteins (Bentov et al., 2010), all of which are potentially present in the cytoplasm of *G. lithophora*. Here we show that the presence of Sr and Ba in addition to Mg might be one additional parameter increasing the stability of poorly crystalline carbonate inclusions in *G. lithophora*.

The cyanobacterium *Candidatus* G. lithophora precipitates poorly crystalline carbonate nanoparticles rich in Sr and Ba. All of these features could be reproduced in the present in vitro experiments. For that purpose, highly supersaturated solutions with significant Sr and Ba concentrations were used. Indeed, the fractionation between the solution and amorphous carbonates was always approximately the same for Sr, Ba and Ca, suggesting that the Sr/Ca and Ba/Ca ratios in the carbonates are about the same as in the precipitating solution. Since Couradeau et al. (2012) measured Sr/Ca and Ba/Ca atomic ratios of 0.14 and 0.39 respectively in the carbonate inclusions of *G. lithophora*, it can be inferred that the cytoplasm of *G. lithophora*, or alternatively the solution in putative vesicles in which these inclusions may form, has the same Sr/Ca and Ba/Ca ratios as the inclusions. These ratios are 86 and 1370 times higher than the respective Sr/Ca and Ba/Ca ratios of the extracellular solution in which *G. lithophora* cells were grown (Couradeau et al., 2012). Therefore, there must be a

mechanism inducing concentration of Sr and Ba over Ca between the extracellular and the intracellular medium of *G. lithophora*.

A few previous studies have shown an enrichment in Sr or Ba over Ca in biological systems. For example, distribution coefficients of Sr and Ba are different in coccoliths of *Emiliania huxleyi* compared to inorganically precipitated calcite (Langer et al., 2006; Payne et al., 2008; Langer et al., 2009). This has been interpreted as the result of the compartmentation of *E. huxleyi* cytoplasm and the functioning of specific transporters, which accumulate Sr and Ba in the vesicles where coccoliths are formed.

Similarly, selective sequestration of Sr has also been observed in the desmid green alga *Closterium moniliferum* (Krejci et al., 2011). Krejci et al. (2011) suggested that Ca and Sr were transported inward and outward of the cells by the same channels but since the precipitates formed by these cells were sulfates, they favored the hypothesis that concentration of Sr over Ca was the result of the lower solubility of Sr-sulfates compared to Ca-sulfates. In other word, they suggested that differential fractionation of Sr and Ca between the extracellular solution and the solids was due to mineral precipitation and not biological transport processes as in the coccolith scenario. Since no precursor Sr-, Ca-, or Ba-sulfate phase could be detected in *G. lithophora*, and since the partitioning between the solution and amorphous carbonates is approximately the same for Ca, Sr and Ba, we favor the hypothesis that there are channels and/or transporters which transport Ca, Sr and Ba at different rates in *G. lithophora*. The regulation of intracellular Ca^{2+} concentration results from the balance between Ca^{2+} influx via channels and Ca^{2+} efflux via active transporters (Waditee et al., 2004). Several Ca^{2+} transporters have been identified and studied (e.g., Waditee et al., 2004; Jiang et al., 2013), but their chemical selectivity will need to be characterized in the future.

Sr/Ca and Ba/Ca ratios in carbonates have often been used as proxies to reconstruct paleoenvironment (e.g., Kunioka et al., 2006; Meibom et al., 2008). The possibility that some biological processes alter these signals is thus important to evaluate.

5. CONCLUSIONS

We produced *in vitro* carbonates with the same shape, size, and chemical composition as those observed in *G. lithophora*. While the poor crystallinity, the shape and the small size may also be impacted by the macromolecules contained within the cells, the present experiments suggest that Sr/Ca and Ba/Ca ratios were the same in the cytoplasm as in amorphous carbonate inclusions, therefore requiring some mechanisms concentrating Sr and Ba over Ca between the extracellular and intracellular medium of the cells. This kind of *in vitro* approach shows that intracellular inclusions found within bacteria can provide some keys to the chemical composition of the intracellular solution in these bacteria.

ACKNOWLEDGMENTS

The authors thank David Montero, Institut des Matériaux de Paris Centre and Région Ile-de-France for SEM-EDXS analyses and Guillaume Morin for help in diffractogram interpretation.

Nithavong Cam was supported by French state funds managed by the ANR within the Investissements d'Avenir programme under reference ANR-11-IDEX-0004-02, and more specifically within the framework of the Cluster of Excellence MATISSE.

Karim Benzerara has been supported by funding from the European Research Council under the European Community's Seventh Framework Programme (FP7/2007-2013 Grant Agreement no.307110 - ERC CALCYAN).

The TEM facility at IMPMC was purchased owing to a support by Region Ile-de-France grant SESAME 2000 E 1435. The SEM facility at IMPMC was purchased owing to a support by Région Ile de France grant SESAME 2006 I-07-593/R.

REFERENCES

Aizenberg J., Lambert G., Addadi L. and Weiner S. (1996) Stabilization of amorphous calcium carbonate by specialized macromolecules in biological and synthetic precipitates. *Adv. Mater.* **8**, 222–226.

Badger M. R. and Andrews T. J. (1982) Photosynthesis and Inorganic Carbon Usage by the Marine Cyanobacterium, Synechococcus sp. *Plant Physiol.* **70**, 517–523.

Badger M. R., Price G. D., Long B. M. and Woodger F. J. (2006) The environmental plasticity and ecological genomics of the cyanobacterial CO_2 concentrating mechanism. *J. Exp. Bot.* **57**, 249–265.

Barrán-Berdón A. L., Rodea-Palomares I., Leganés F. and Fernández-Piñas F. (2011) Free Ca^{2+} as an early intracellular biomarker of exposure of cyanobacteria to environmental pollution. *Anal. Bioanal. Chem.* **400**, 1015–1029.

Belkin S. and Boussiba S. (1991) High internal pH conveys ammonia resistance in spirulina platensis. *Bioresour. Technol.* **38**, 167–169.

Bentov S., Weil S., Glazer L., Sagi A. and Berman A. (2010) Stabilization of amorphous calcium carbonate by phosphate rich organic matrix proteins and by single phosphoamino acids. *J. Struct. Biol.* **171**, 207–215.

Benzerara K., Skouri-Panet F., Li J., Férard C., Gugger M., Laurent T., Couradeau E., Ragon M., Cosmidis J., Menguy N., Margaret-Oliver I., Tavera R., López-García P. and Moreira D. (2014) Intracellular Ca-carbonate biomineralization is widespread in cyanobacteria. *Proc. Natl. Acad. Sci.* **111**, 10933–10938.

Brečević L. and Nielsen A. E. (1989) Solubility of amorphous calcium carbonate. *J. Cryst. Growth* **98**, 504–510.

Cartwright J. H. E., Checa A. G., Gale J. D., Gebauer D. and Sainz-Díaz C. I. (2012) Calcium Carbonate Polyamorphism and Its Role in Biomineralization: How Many Amorphous Calcium Carbonates Are There? *Angew. Chem. Int. Ed.* **51**, 11960–11970.

Couradeau E., Benzerara K., Gerard E., Moreira D., Bernard S., Brown G. E. and Lopez-Garcia P. (2012) An Early-Branching Microbialite Cyanobacterium Forms Intracellular Carbonates. *Science* **336**, 459–462.

Dietzel M. and Usdowski E. (1996) Coprecipitation of Ni^{2+}, Co^{2+}, and Mn^{2+} with galena and covellite, and of Sr^{2+} with calcite during crystallization via diffusion of H_2S and CO_2 through polyethylene at 20°C: Power law and Nernst law control of trace element partitioning. *Chem. Geol.* **131**, 55–65.

Dietzel M., Gussone N. and Eisenhauer A. (2004) Co-precipitation of Sr^{2+} and Ba^{2+} with aragonite by membrane diffusion of CO_2 between 10 and 50 °C. *Chem. Geol.* **203**, 139–151.

Fernandez-Martinez A., Kalkan B., Clark S. M. and Waychunas G. A. (2013) Pressure-Induced Polyamorphism and Formation of "Aragonitic" Amorphous Calcium Carbonate. *Angew. Chem. Int. Ed.* **52**, 8354–8357.

Fuhrman J. (2003) Genome sequences from the sea. *Nature* **424**, 1001–1002.

Gebauer D., Völkel A. and Cölfen H. (2008) Stable Prenucleation Calcium Carbonate Clusters. *Science* **322**, 1819–1822.

Gebauer D., Gunawidjaja P. N., Ko J. Y. P., Bacsik Z., Aziz B., Liu L., Hu Y., Bergström L., Tai C.-W., Sham T.-K., Edén M. and Hedin N. (2010) Proto-Calcite and Proto-Vaterite in Amorphous Calcium Carbonates. *Angew. Chem. Int. Ed.* **49**, 8889–8891.

Gebrehiwet T. A., Redden G. D., Fujita Y., Beig M. S. and Smith R. W. (2012) The Effect of the CO_3^{2-} to Ca^{2+} Ion activity ratio on calcite precipitation kinetics and Sr^{2+} partitioning. *Geochem. Trans.* **13**, 1.

Ihli J., Kulak A. N. and Meldrum F. C. (2013a) Freeze-drying yields stable and pure amorphous calcium carbonate (ACC). *Chem. Commun.* **49**, 3134.

Ihli J., Kim Y.-Y., Noel E. H. and Meldrum F. C. (2013b) The Effect of Additives on Amorphous Calcium Carbonate (ACC): Janus Behavior in Solution and the Solid State. *Adv. Funct. Mater.* **23**, 1575–1585.

Jaquet J.-M., Nirel P. and Martignier A. (2013) Preliminary investigations on picoplankton-related precipitation of alkaline-earth metal carbonates in meso-oligotrophic lake Geneva (Switzerland). *J. Limnol.* **72**, 592–605.

Jiang H.-B., Cheng H.-M., Gao K.-S. and Qiu B.-S. (2013) Inactivation of Ca^{2+}/H^+ Exchanger in Synechocystis sp. Strain PCC 6803 Promotes Cyanobacterial Calcification by Upregulating CO_2-Concentrating Mechanisms. *Appl. Environ. Microbiol.* **79**, 4048–4055.

Jiang J., Gao M.-R., Qiu Y.-H. and Yu S.-H. (2010) Gram-scale, low-cost, rapid synthesis of highly stable Mg–ACC nanoparticles and their long-term preservation. *Nanoscale* **2**, 2358–2361.

Kamennaya N. A., Ajo-Franklin C. M., Northen T. and Jansson C. (2012) Cyanobacteria as Biocatalysts for Carbonate Mineralization. *Minerals* **2**, 338–364.

Kellermeier M., Picker A., Kempter A., Cölfen H. and Gebauer D. (2014) A Straightforward Treatment of Activity in Aqueous $CaCO_3$ Solutions and the Consequences for Nucleation Theory. *Adv. Mater.* **26**, 752–757.

Kinsman D. J. J. and Holland H. D. (1969) The co-precipitation of cations with $CaCO_3$—IV. The co-precipitation of Sr^{2+} with aragonite between 16° and 96°C. *Geochim. Cosmochim. Acta* **33**, 1–17.

Kitano Y. and Hood D. W. (1965) The influence of organic material on the polymorphic crystallization of calcium carbonate. *Geochim. Cosmochim. Acta* **29**, 29–41.

Koga N., Nakagoe Y. and Tanaka H. (1998) Crystallization of amorphous calcium carbonate. *Thermochim. Acta* **318**, 239–244.

Krejci M. R., Wasserman B., Finney L., McNulty I., Legnini D., Vogt S. and Joester D. (2011) Selectivity in biomineralization of barium and strontium. *J. Struct. Biol.* **176**, 192–202.

Kunioka D., Shirai K., Takahata N., Sano Y., Toyofuku T. and Ujiie Y. (2006) Microdistribution of Mg/Ca, Sr/Ca, and Ba/Ca ratios in Pulleniatina obliquiloculata test by using a NanoSIMS: Implication for the vital effect mechanism. *Geochem. Geophys. Geosystems* **7**, Q12P20.

Kupriyanova E. V. and Pronina N. A. (2011) Carbonic anhydrase: Enzyme that has transformed the biosphere. *Russ. J. Plant Physiol.* **58**, 197–209.

Langer G., Gussone N., Nehrke G., Riebesell U., Eisenhauer A., Kuhnert H., Rost B., Trimborn S. and Thoms S. (2006) Coccolith strontium to calcium ratios in Emiliania huxleyi: The dependence on seawater strontium and calcium concentrations. *Limnol. Oceanogr.* **51**, 310–320.

Langer G., Nehrke G., Thoms S. and Stoll H. (2009) Barium partitioning in coccoliths of Emiliania huxleyi. *Geochim. Cosmochim. Acta* **73**, 2899–2906.

Levi-Kalisman Y., Raz S., Weiner S., Addadi L. and Sagi I. (2000) X-Ray absorption spectroscopy studies on the structure of a biogenic "amorphous" calcium carbonate phase. *J. Chem. Soc. Dalton Trans.*, 3977–3982.

Liu Y.-Y., Jiang J., Gao M.-R., Yu B., Mao L.-B. and Yu S.-H. (2013) Phase Transformation of Magnesium Amorphous Calcium Carbonate (Mg-ACC) in a Binary Solution of Ethanol and Water. *Cryst. Growth Des.* **13**, 59–65.

Lorens R. B. (1981) Sr, Cd, Mn and Co distribution coefficients in calcite as a function of calcite precipitation rate. *Geochim. Cosmochim. Acta* **45**, 553–561.

Loste E., Wilson R. M., Seshadri R. and Meldrum F. C. (2003) The role of magnesium in stabilising amorphous calcium carbonate and controlling calcite morphologies. *J. Cryst. Growth* **254**, 206–218.

Meibom A., Cuif J.-P., Houlbreque F., Mostefaoui S., Dauphin Y., Meibom K. L. and Dunbar R. (2008) Compositional variations at ultra-structure length scales in coral skeleton. *Geochim. Cosmochim. Acta* **72**, 1555–1569.

Meldrum F. C. and Sear R. P. (2008) Now You See Them. *Science* **322**, 1802–1803.

Merz M. U. (1992) The biology of carbonate precipitation by cyanobacteria. *Facies* **26**, 81–101.

Michel F. M., MacDonald J., Feng J., Phillips B. L., Ehm L., Tarabrella C., Parise J. B. and Reeder R. J. (2008) Structural Characteristics of Synthetic Amorphous Calcium Carbonate. *Chem. Mater.* **20**, 4720–4728.

Mucci A. and Morse J. W. (1983) The incorporation of Mg^{2+} and Sr^{2+} into calcite overgrowths: influences of growth rate and solution composition. *Geochim. Cosmochim. Acta* **47**, 217–233.

Navrotsky A. (2004) Energetic clues to pathways to biomineralization: Precursors, clusters, and nanoparticles. *Proc. Natl. Acad. Sci. U. S. A.* **101**, 12096–12101.

Payne V. E., Rickaby R. E. M., Benning L. G. and Shaw S. (2008) Calcite crystal growth orientation: implications for trace metal uptake into coccoliths. *Mineral. Mag.* **72**, 269–272.

Pingitore Jr. N. E. and Eastman M. P. (1986) The coprecipitation of Sr^{2+} with calcite at 25°C and 1 atm. *Geochim. Cosmochim. Acta* **50**, 2195–2203.

Politi Y., Metzler R. A., Abrecht M., Gilbert B., Wilt F. H., Sagi I., Addadi L., Weiner S. and Gilbert P. (2008) Transformation mechanism of amorphous calcium carbonate into calcite in the sea urchin larval spicule. *Proc. Natl. Acad. Sci.* **105**, 17362–17366.

Radha A. V., Forbes T. Z., Killian C. E., Gilbert P. U. P. A. and Navrotsky A. (2010) Transformation and crystallization energetics of synthetic and biogenic amorphous calcium carbonate. *Proc. Natl. Acad. Sci.* **107**, 16438–16443.

Radha A. V., Fernandez-Martinez A., Hu Y., Jun Y.-S., Waychunas G. A. and Navrotsky A. (2012) Energetic and structural studies of amorphous $Ca_{1-x}Mg_xCO_3{\cdot}nH_2O$ ($0 \le x \le 1$). *Geochim. Cosmochim. Acta* **90**, 83–95.

Raiteri P. and Gale J. D. (2010) Water Is the Key to Nonclassical Nucleation of Amorphous Calcium Carbonate. *J. Am. Chem. Soc.* **132**, 17623–17634.

Riding R. (2012) A Hard Life for Cyanobacteria. *Science* **336**, 427–428.

Rimstidt J. D., Balog A. and Webb J. (1998) Distribution of trace elements between carbonate minerals and aqueous solutions. *Geochim. Cosmochim. Acta* **62**, 1851–1863.

Rodriguez-Blanco J. D., Shaw S., Bots P., Roncal-Herrero T. and Benning L. G. (2012) The role of pH and Mg on the stability and crystallization of amorphous calcium carbonate. *J. Alloys Compd.* **536**, S477–S479.

Sel O., Radha A. V., Dideriksen K. and Navrotsky A. (2012) Amorphous iron (II) carbonate: Crystallization energetics and comparison to other carbonate minerals related to CO_2 sequestration. *Geochim. Cosmochim. Acta* **87**, 61–68.

Stephens C. J., Ladden S. F., Meldrum F. C. and Christenson H. K. (2010) Amorphous Calcium Carbonate is Stabilized in Confinement. *Adv. Funct. Mater.* **20**, 2108–2115.

Tesoriero A. J. and Pankow J. F. (1996) Solid solution partitioning of Sr^{2+}, Ba^{2+}, and Cd^{2+} to calcite. *Geochim. Cosmochim. Acta* **60**, 1053–1063.

Thompson J. B., Schultze-Lam S., Beveridge T. J. and Des Marais D. J. (1997) Whiting events: biogenic origin due to the photosynthetic activity of cyanobacterial picoplankton. *Limnol. Oceanogr.* **42**, 133–141.

Verrecchia E., Freytet P., Verrecchia K. and Dumont J. (1995) Spherulites in Calcrete Laminar Crusts - Biogenic $CaCO_3$ Precipitation. *J. Sediment. Res. Sect. -Sediment. Petrol. Process.* **65**, 690–700.

Waditee R., Hossain G. S., Tanaka Y., Nakamura T., Shikata M., Takano J., Takabe T. and Takabe T. (2004) Isolation and Functional Characterization of Ca^{2+}/H^+ Antiporters from Cyanobacteria. *J. Biol. Chem.* **279**, 4330–4338.

Weiner S. and Addadi L. (2011) Crystallization Pathways in Biomineralization. *Annu. Rev. Mater. Res.* **41**, 21–40.

Yu X.-C. and Margolin W. (1997) Ca^{2+}-mediated GTP-dependent dynamic assembly of bacterial cell division protein FtsZ into asters and polymer networks in vitro. *EMBO J.* **16**, 5455–5463.

FIGURE CAPTIONS

Fig. 1. Characterization of the solid products formed in the synthesis with stoichiometric conditions at high carbonate concentration (100 mM) with Na_2CO_3 as a carbonate source. A) Bright-field TEM image of the poorly crystalline carbonate particles. B) EDXS spectrum of the particles. Sodium and chlorine are attributed to salt precipitating upon drying. Mg, Ca, Sr and Ba are detected within the particles. C) MS coupled TGA-DSC analyses of the poorly crystalline Ca, Mg, Sr, Ba-carbonates formed at high carbonate concentration. DTG curve (full line), released CO_2 (dash line) and heat flow curve (dot line) are plotted against heating temperature. D) XRD patterns of the sample dried at room temperature immediately after the mixing of the solutions (i), after heating at 325 °C (ii), at 375 °C (iii) and sample dried one month after mixing of the solutions (iv). “h” denotes diffraction peaks attributed to halite NaCl (peaks at 32°and 47° in 2θ are attributed to the (200) and (220) planes, respectively). “c” denotes diffraction peaks attributed to calcite. Diffraction peaks at 23, 29 and 36° are attributed to the (012), (104) and (110) calcite planes respectively.

Fig. 2. Characterization of the solid products of the synthesis with stoichiometric conditions at high carbonate concentration (100 mM) and with $NaHCO_3$ as a carbonate source. A) EDXS spectrum of the product. Sodium and chloride result from residual salt formed upon sample drying. B) XRD pattern of the sample. "h" stands for halite diffraction peaks; "c" for calcite. The diffraction peaks at 23, 29 and 36° are attributed to the (012), (104) and (110) calcite planes, respectively.

Fig. 3. Characterization of the solid products of the synthesis under stoichiometric conditions performed at low carbonate concentration (10 mM). A) Bright-field TEM image of the particles. B) EDXS spectrum of the particles. Sodium and chloride result from residual salt formed upon sample drying. Mg, Ca, Sr and Ba are detected within the particles. C) TGA-DSC analyses of the poorly crystalline Ca, Mg, Sr, Ba-carbonates formed at low carbonate concentration. DTG curve (full line), and heat flow curve (dot line) are plotted against heating temperature. D) XRD patterns of the sample dried at room temperature immediately after the mixing of the solutions (i), washed with milliQ water (ii) and collected one month after the precipitation (iii). "v" stands for vaterite diffraction peaks, "m" for monohydrocalcite and "c" for calcite. The diffraction peaks at 23, 29 and 36° are attributed to the (012), (104) and (110) calcite planes, respectively.

Fig. 4. Characterization of the solid products of the synthesis performed at low carbonate concentration (10 mM) with a high magnesium concentration (10 mM). A) Bright-field TEM image of the particles. B) EDXS spectrum of the particles. Sodium and chloride result from residual salt formed upon sample drying. Mg, Ca, Sr and Ba are detected within the particles. C) TGA-DSC analyses of the poorly crystalline Ca, Mg, Sr, Ba-carbonates. DTG curve (full line), and heat flow curve (dot line) are plotted against heating temperature. D) XRD patterns of the poorly crystalline sample dried at room temperature immediately after the mixing of the solutions.

Fig. 5. Characterization of the solid products of the synthesis performed at low carbonate concentration (10 mM) without magnesium. A) SEM image of the particles. B) EDXS spectrum of the particles. Sodium and chloride result from residual salt formed upon sample drying. C) TGA-DSC analyses of the crystalline carbonates. DTG curve (full line), and heat flow curve (dot line) are plotted against heating temperature. D) XRD patterns of sample. "c" denotes diffraction peaks attributed to calcite. Diffraction peaks at 23, 29 and 36° are attributed to the (012), (104) and (110) calcite planes respectively.

Fig. 6. Characterization of the solid products of the synthesis performed at low carbonate concentration (10 mM) with a high magnesium concentration (10 mM) and without strontium. A) Bright-field TEM image of the particles. B) EDXS spectrum of the particles. Sodium and chloride result from residual salt formed upon sample drying. Mg, Ca and Ba are detected within the particles. C) TGA-DSC analyses of the poorly crystalline Ca, Mg, Ba-carbonates. DTG curve (full line), and heat flow curve (dot line) are plotted against heating temperature. D) XRD patterns of the sample dried at room temperature immediately after the mixing of the solutions (i) and collected one month after the precipitation (ii). "m" denotes diffraction peaks attributed to monohydrocalcite. Diffraction peaks at 20.5, 29 and 31.7° are attributed to the (111) and (2-11) monohydrocalcite planes for 20.5°, (112) and (2-12) for 29°, (031) and (301) for 31.7°.

Fig. 7. Characterization of the solid products of the synthesis performed at low carbonate concentration (10 mM) with a high magnesium concentration (10 mM) and without barium. A) Bright-field TEM image of the particles. B) EDXS spectrum of the particles. Sodium and chlorine result from residual salt formed upon sample drying. Mg, Ca and Sr are detected within the particles. C) TGA-DSC analyses of the poorly crystalline Ca, Mg, Sr-carbonates. DTG curve (full line), and heat flow curve (dot line) are plotted against heating temperature. D) XRD patterns of the sample dried at room temperature immediately after the mixing of the

solutions (i) and collected one month after the precipitation (ii). “m” stands for monohydrocalcite diffraction peaks and “a” for aragonite. Diffraction peaks at 20.5, 29 and 31.7° are attributed to the (111) and (2-11) monohydrocalcite planes for 20.5°, (112) and (2-12) for 29, (031) and (301) for 31.7°. The diffraction peaks at 26 and 27° are attributed to the (111) and (021) aragonite planes, respectively.

Fig. 8. Characterization of the solid products of the synthesis performed at low carbonate concentration (10 mM) with a high magnesium concentration (10 mM) and without strontium and barium. A) SEM image of the particles. B) EDXS spectrum of the particles. Sodium and chlorine result from residual salt formed upon sample drying. C) XRD patterns of the sample dried at room temperature immediately after the mixing of the solutions. “m” denotes diffraction peaks attributed to monohydrocalcite. Diffraction peaks at 20.5, 29 and 31.7° are attributed to the (111) and (2-11) monohydrocalcite planes for 20.5°, (112) and (2-12) for 29°, (031) and (301) for 31.7°.

Table 1: List of performed experiments, indicating the concentrations of the different elements before precipitation and the chemical and mineralogical compositions of the resulting precipitates. All of these experiments were carried out at room temperature. The elemental ratios were determined by EDXS and the water quantity was inferred from TGA analyses. The final pH corresponds to the pH measured about 15 min after the precipitation. The saturation indices of the solutions with amorphous calcium carbonate have been calculated based on the solubility product measured by Kellermeier et al. (2014)

Table

Experiments	Initial concentrations (in mM)					Saturation indices		Final pH	Mineral composition	Chemical composition
	$[Mg^{2+}]$	$[Ca^{2+}]$	$[Sr^{2+}]$	$[Ba^{2+}]$	$[CO_3^{2-}]$	Calcite	ACC			
Stoichiometric conditions at high concentrations (Fig.1)	18.5	53.1	7.7	20.8	100	3.857	3.012	10.63	Amorphous	$Mg_{0.16}Ca_{0.51}Sr_{0.08}Ba_{0.25}CO_3 \cdot 0.86H_2O$
Stoichiometric conditions at low concentrations (Fig.3)	1.85	5.31	0.77	2.08	10	2.758	1.913	11.02	Amorphous	$Mg_{0.04}Ca_{0.61}Sr_{0.06}Ba_{0.29}CO_3 \cdot 0.84H_2O$
Higher Mg concentration (Fig.4)	10	5.31	0.77	2.08	10	2.648	1.803	10.64	Amorphous	$Mg_{0.16}Ca_{0.51}Sr_{0.05}Ba_{0.28}CO_3 \cdot 1.03H_2O$
Without Mg (Fig.5)	0	5.31	0.77	2.08	10	2.783	1.938	10.88	Calcite	$Ca_{0.59}Sr_{0.07}Ba_{0.34}CO_3$
Without Sr (Fig.6)	10	5.31	0	2.08	10	2.657	1.812	10.57	Amorphous	$Mg_{0.16}Ca_{0.56}Ba_{0.28}CO_3 \cdot 0.93H_2O$
Without Ba (Fig.7)	10	5.31	0.77	0	10	2.669	1.824	10.64	Amorphous	$Mg_{0.25}Ca_{0.67}Sr_{0.08}CO_3 \cdot 0.88H_2O$
Without Sr and Ba (Fig.8)	10	5.31	0	0	10	2.678	1.833	10.68	Monohydrocalcite	$(Mg_{0.26}Ca_{0.74})CO_3 \cdot 1.6H_2O$

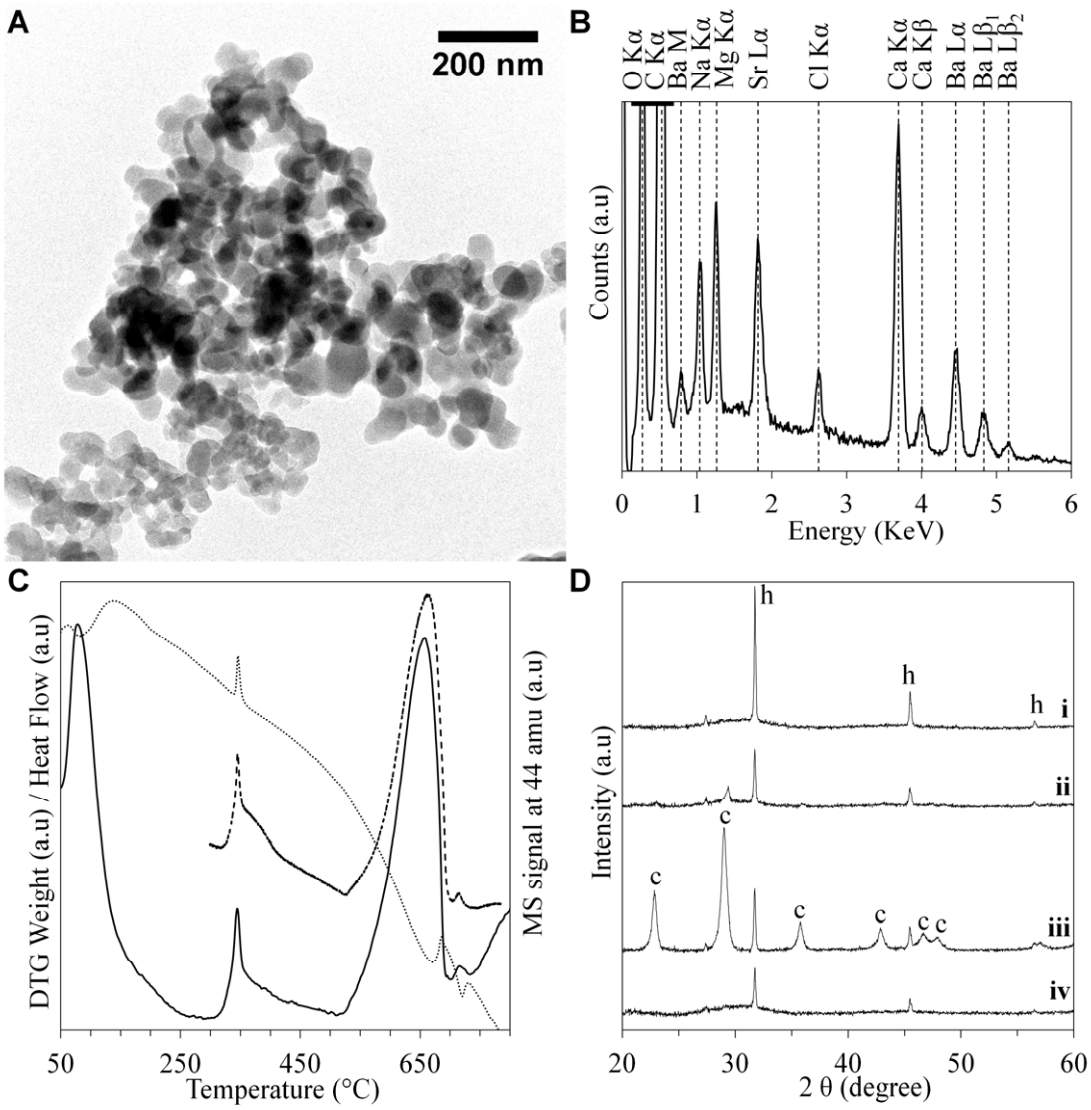

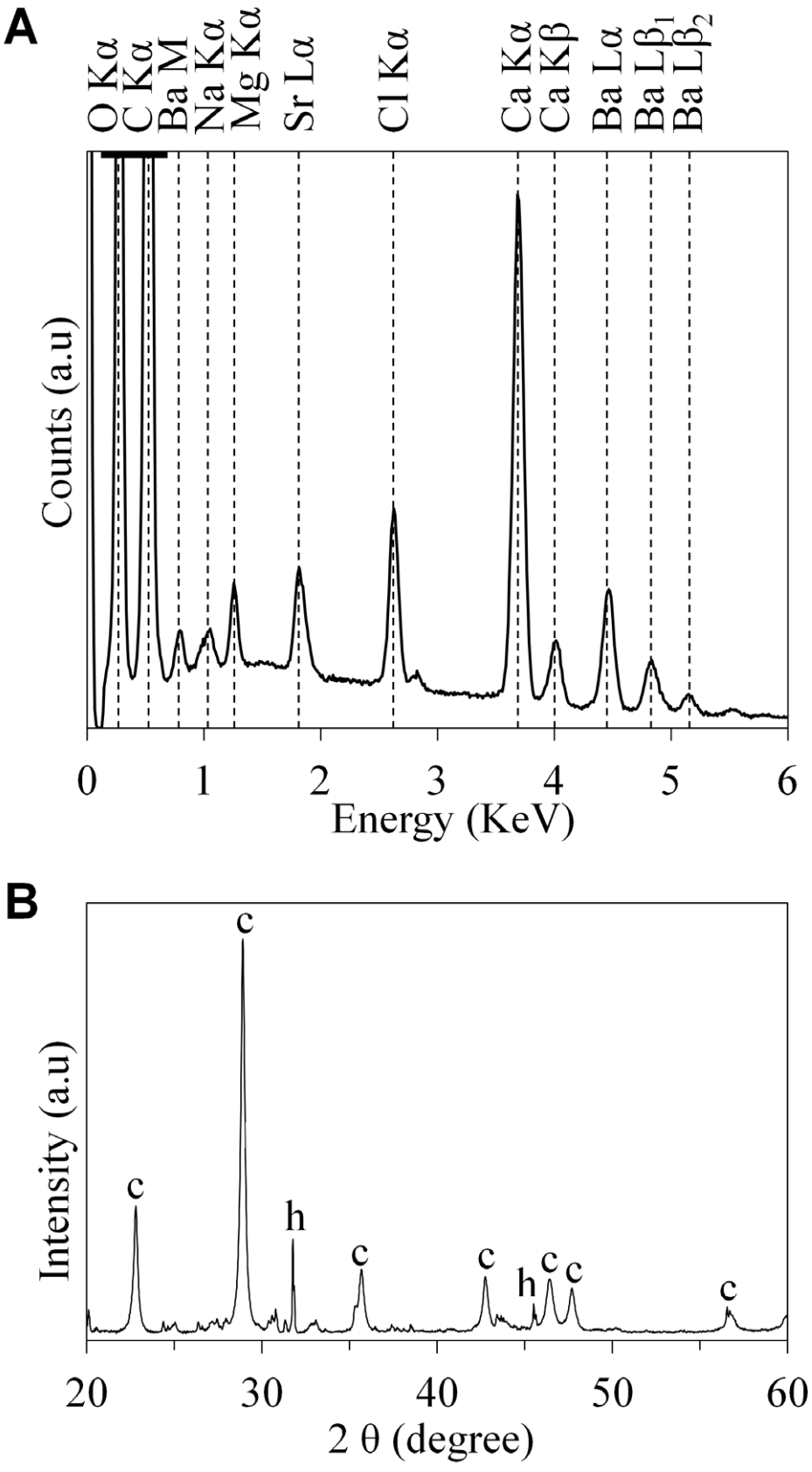
A
O Kα
C Kα
Ba M
Na Kα
Mg Kα
Sr Lα
Cl Kα
Ca Kα
Ca Kβ
Ba Lα
Ba Lβ1
Ba Lβ2
Counts (a.u)
0
1
2
3
4
5
6
Energy (KeV)
B
Intensity (a.u)
c
c
h
c
c
h
c
c
c
20
30
40
50
60
2 θ (degree)

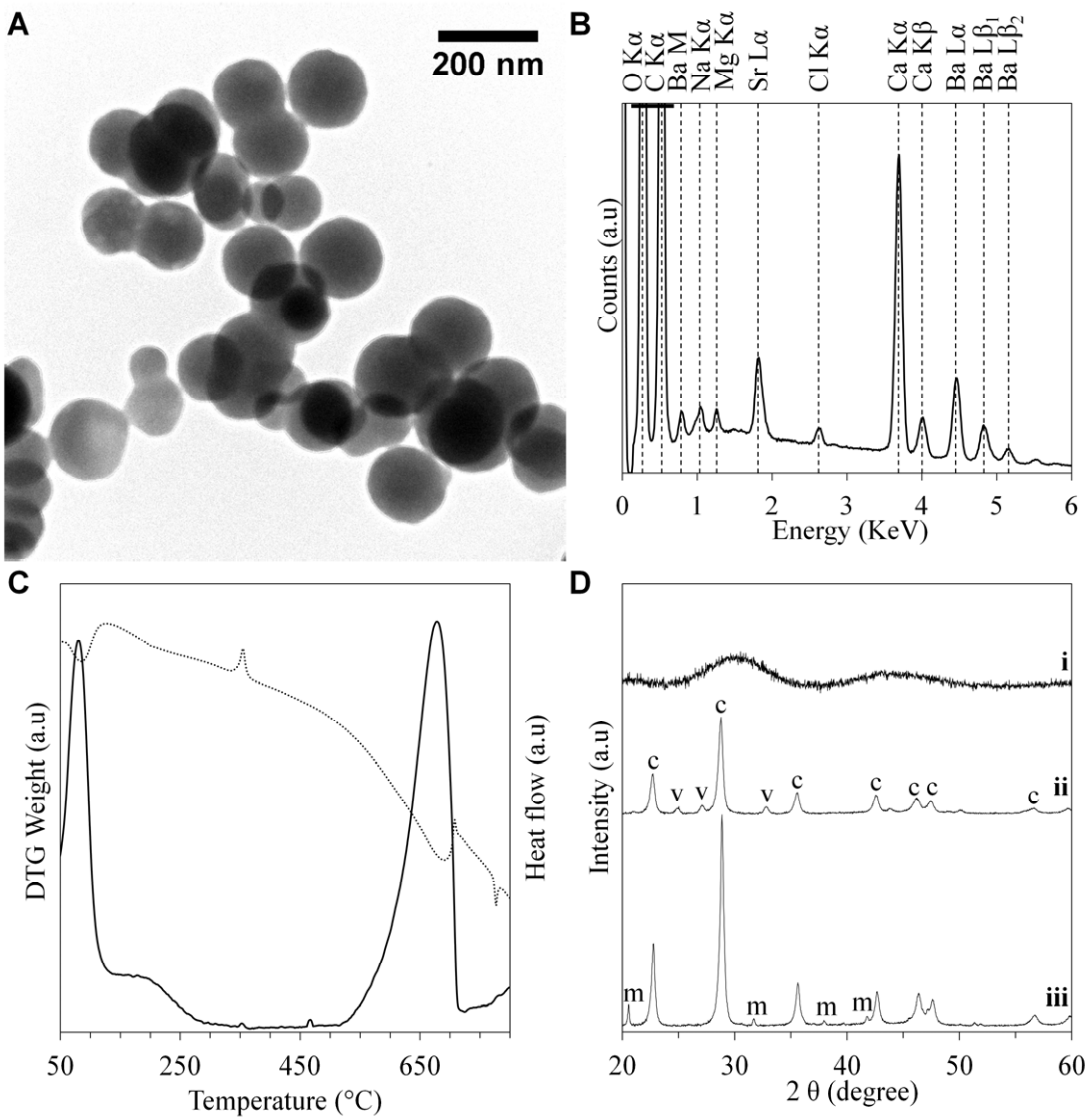

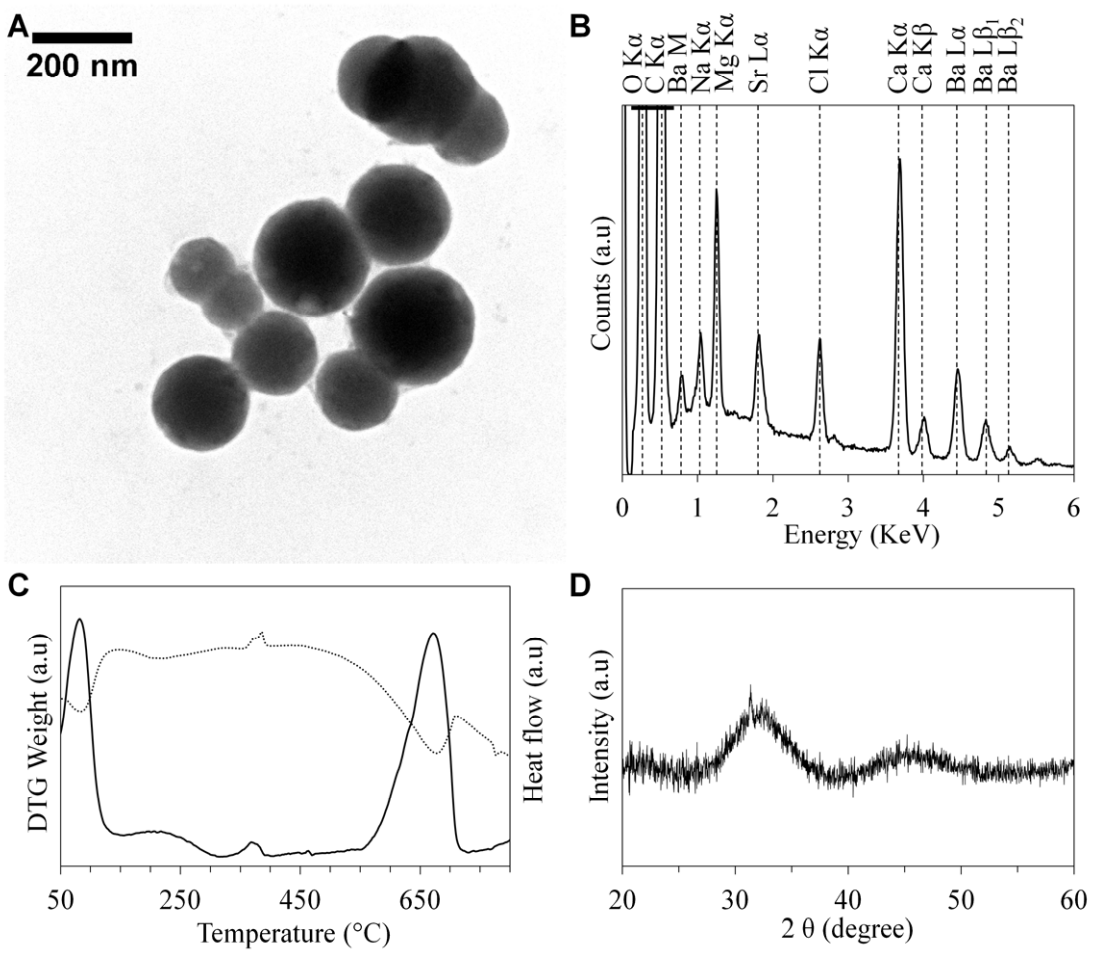
A
200 nm
B
O Kα
C Kα
Ba M
Na Kα
Mg Kα
Sr Lα
Cl Kα
Ca Kα
Ca Kβ
Ba Lα
Ba Lβ1
Ba Lβ2
Counts (a.u)
0
1
2
3
4
5
6
Energy (KeV)
C
DTG Weight (a.u)
Heat flow (a.u)
50
250
450
650
Temperature (°C)
D
Intensity (a.u)
20
30
40
50
60
2 θ (degree)

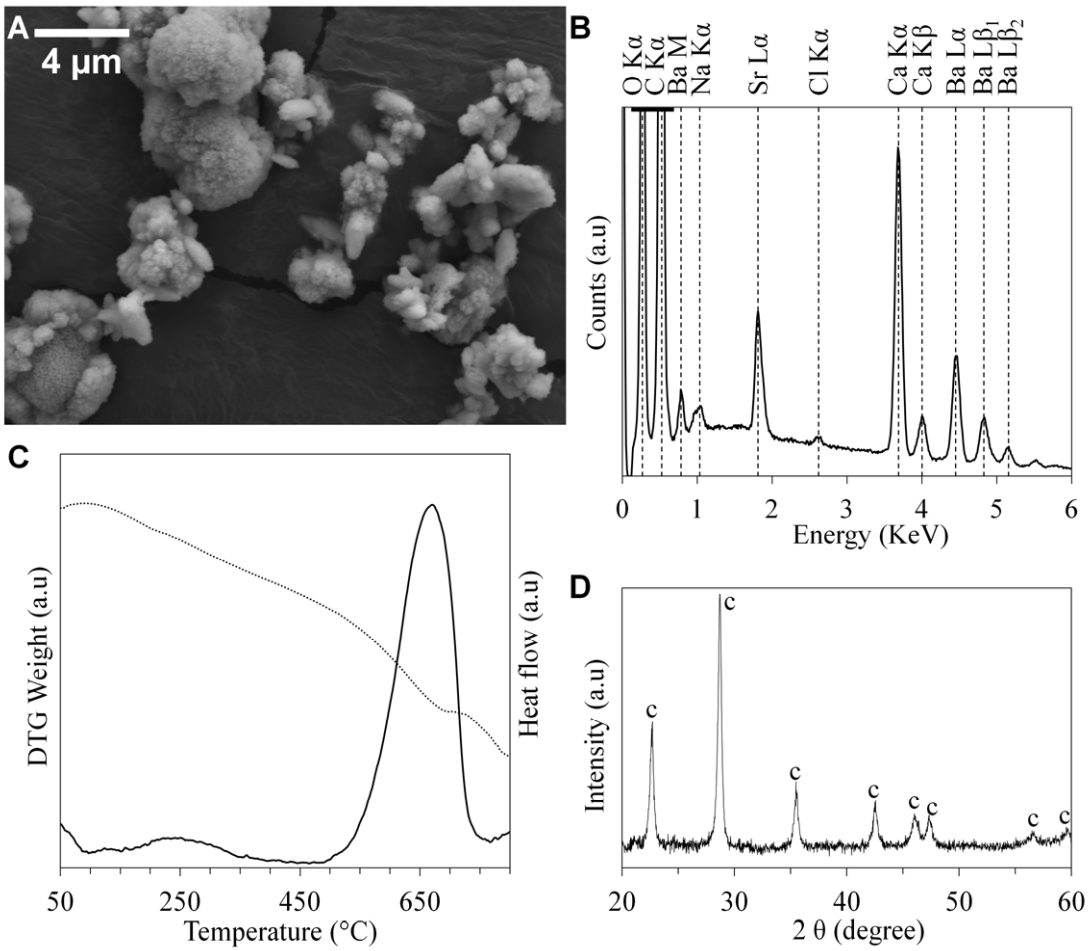
A
4 µm
B
O Kα
C Kα
Ba M
Na Kα
Sr Lα
Cl Kα
Ca Kα
Ca Kβ
Ba Lα
Ba Lβ1
Ba Lβ2
Counts (a.u)
0
1
2
3
4
5
6
Energy (KeV)
C
DTG Weight (a.u)
Heat flow (a.u)
50
250
450
650
Temperature (°C)
D
Intensity (a.u)
c
20
30
40
50
60
2 θ (degree)

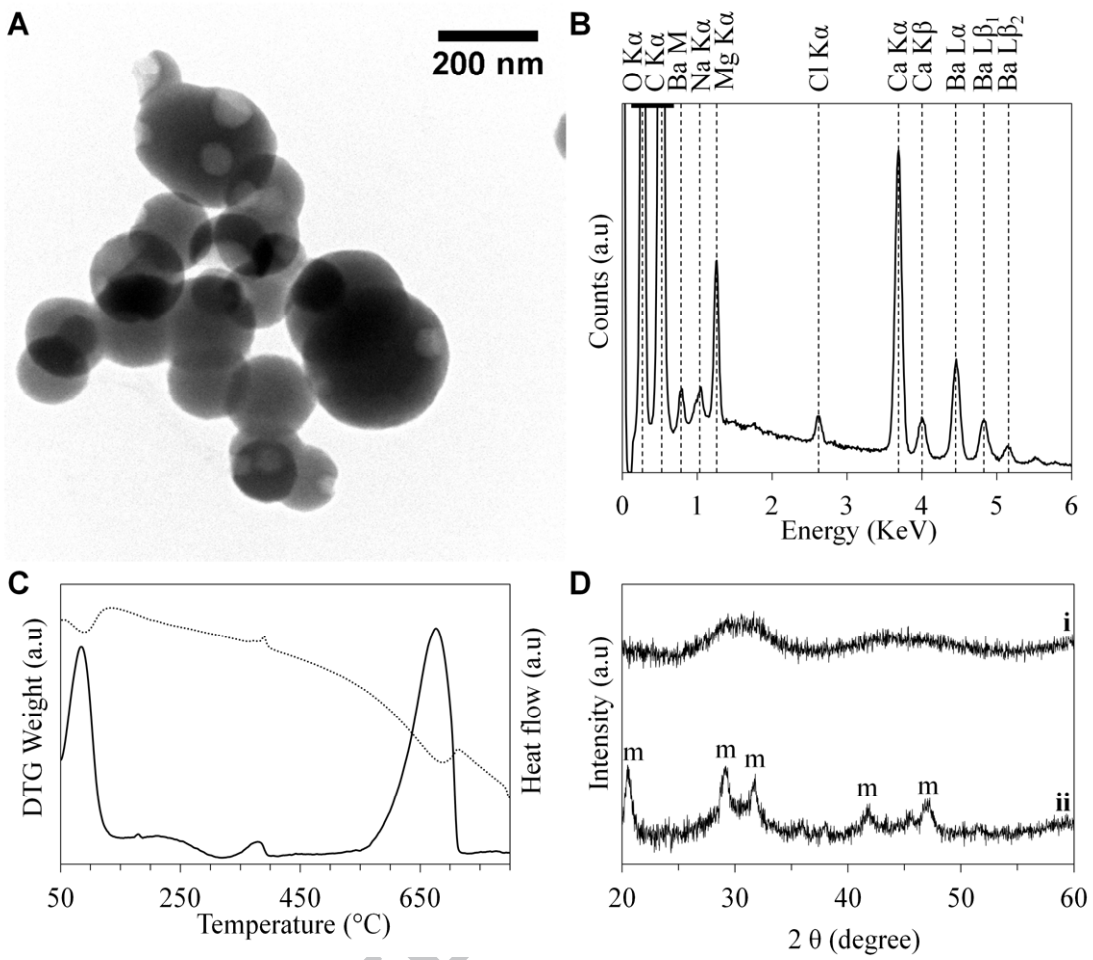
A
200 nm
B
O Kα
C Kα
Ba M
Na Kα
Mg Kα
Cl Kα
Ca Kα
Ca Kβ
Ba Lα
Ba Lβ1
Ba Lβ2
Counts (a.u)
0
1
2
3
4
5
6
Energy (KeV)
C
DTG Weight (a.u)
Heat flow (a.u)
50
250
450
650
Temperature (°C)
D
Intensity (a.u)
i
ii
m
m
m
m
m
20
30
40
50
60
2 θ (degree)

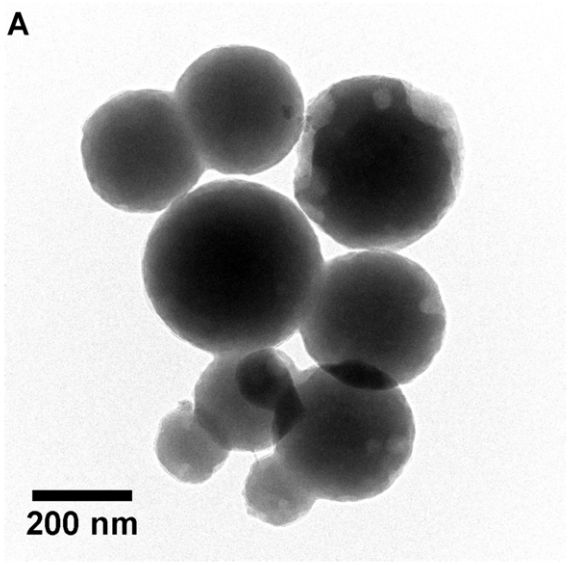
A
200 nm

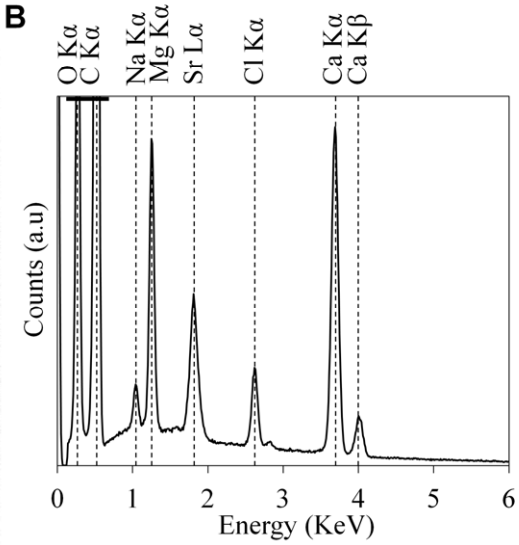
B
O Kα
C Kα
Na Kα
Mg Kα
Sr Lα
Cl Kα
Ca Kα
Ca Kβ
Counts (a.u)
0
1
2
3
4
5
6
Energy (KeV)

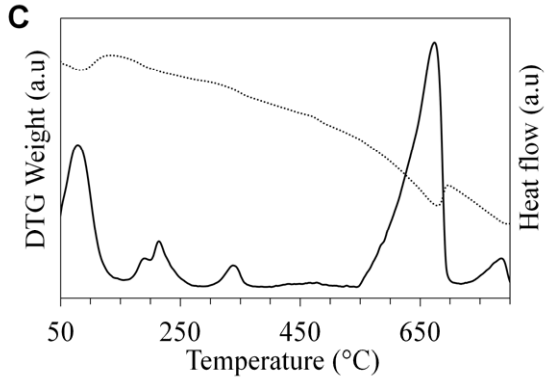
C
DTG Weight (a.u)
Heat flow (a.u)
50
250
450
650
Temperature (°C)

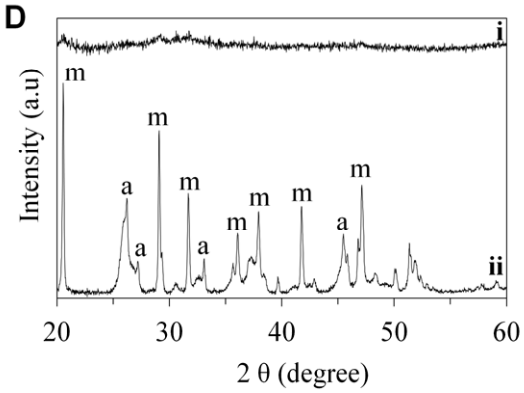
D
i
ii
m
a
Intensity (a.u)
20
30
40
50
60
2 θ (degree)

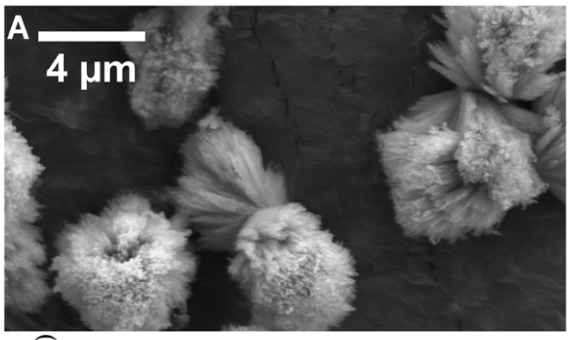
A
4 µm

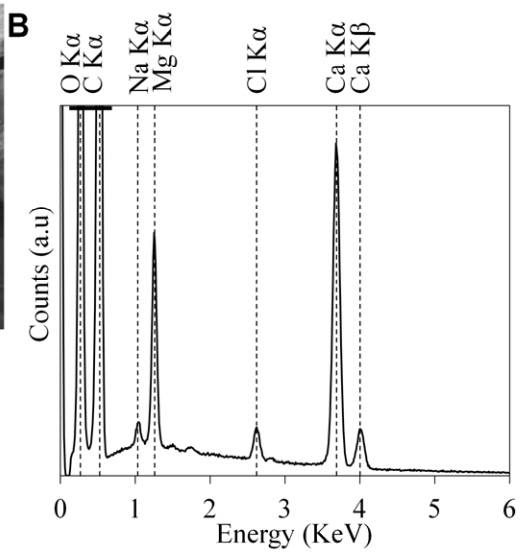
B
O Kα
C Kα
Na Kα
Mg Kα
Cl Kα
Ca Kα
Ca Kβ
Counts (a.u)
0
1
2
3
4
5
6
Energy (KeV)

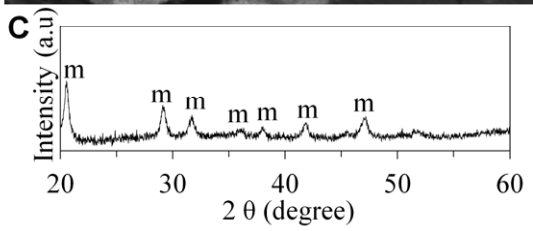
C
Intensity (a.u)
m
20
30
40
50
60
2 θ (degree)